

## Dynamics of collective excitations in $^{190,192}\text{Os}$ and $^{194}\text{Pt}$ observed by 8 MeV neutron scattering

T. B. Clegg,\* G. Haouat, J. P. Delaroche, Ch. Lagrange, and J. Chardine  
*Centre d'Etudes de Bruyères-le-Châtel, 91680, Bruyères-le-Châtel, France*

M. T. McEllistrem, S. E. Hicks,<sup>†</sup> and G. R. Shen<sup>‡</sup>

*Department of Physics and Astronomy, The University of Kentucky, Lexington, Kentucky 40506*

(Received 25 April 1989)

Differential cross sections have been measured for the scattering of 8 MeV neutrons from  $^{190,192}\text{Os}$  and  $^{194}\text{Pt}$ . These measurements have been combined with information from other neutron scattering experiments to fix accurately the electric quadrupole and octupole excitation strengths for low-lying levels. Comparison of this information with electromagnetic excitations for these same nuclei elucidates the rapidly evolving behavior of low-lying collective structures in Pt and Os nuclei. The  $^{194}\text{Pt}$  excitations are those of a nucleus with a potential energy surface very soft to nonaxial deformations. On the other hand, the scattering cross sections for excited levels of  $^{190}\text{Os}$  show evolution of excitations toward those of a nucleus vibrating about a prolate equilibrium shape.

### I. INTRODUCTION

Excitations of nuclei leave their signatures in inelastic scattering cross sections, bound-energy-level spectra, and  $\gamma$ -decay strength patterns. While energy spectra and bound-level decay strengths remain the principal methods for characterizing collectivity, the dependence of nuclear dynamics on increasing excitation energy is best studied by nuclear scattering or reactions. Reactions are especially and distinctively sensitive to nuclear dynamics because of interferences between transition amplitudes for different levels. Such interferences are not present in bound-state transitions.

The Os-Pt mass region is particularly fruitful for testing the sensitivity of scattering to dynamical character because their nuclear structures evolve rapidly from  $A = 190$ – $200$ . Bound-state studies and quadrupole moment measurements show that  $^{194,196}\text{Pt}$  are intrinsically slightly oblate, while the lighter Os nuclei are strongly prolate.

Any scattering study evoking and quantifying the dynamical character of nuclei has several problems not encountered in studies of bound levels. First, the complex nature of low-energy, hadronic interactions means that there is no *a priori* reason to expect that different hadrons will produce excitations with the same strengths. Studies of nucleon scattering from single-closed-shell nuclei<sup>1,2</sup> confirm differences; neutrons and protons excite the same levels, but with slightly different strengths. At least in these spherical nuclei there is enough decoupling of neutron and proton motions to produce small differences. Experience with deformed rotational nuclei is that neutron and proton scattering, and Coulomb excitation with heavy ions all yield the same structural response. This response is characteristic of the excitations and independent of the exciting probe,<sup>3–5</sup> for deformed nuclei.

Scattering studies of nuclear dynamics face two prob-

lems which must be distinguished. One is determining the mean scattering fields in which the incident projectiles and reaction-product wave functions are formed, and the other is determining the transition amplitudes which connect different scattering channels. These transition amplitudes are the signatures of excitations of the target nucleus. Recent low-energy neutron scattering studies<sup>6–8</sup> of Os and Pt nuclei well define the mean scattering fields. Very low-energy strength functions and scattering lengths, total cross sections from 300 keV to 30 MeV, and differential scattering cross sections measured for incident neutron energies below 5 MeV fix the parameters of neutron scattering potentials.

The several previous nucleon scattering studies<sup>6–8</sup> of shape-transitional nuclei were able to discriminate among specific models of the target nuclei,  $^{190,192}\text{Os}$  and  $^{194}\text{Pt}$ . The nuclear structure and dynamics of  $^{190,192}\text{Os}$  and  $^{194}\text{Pt}$  fix the transition amplitudes which couple scattering channels to each other. The previous neutron scattering studies cited are sensitive to and consistent with models which describe all three nuclei as being relatively soft against changes in the  $\gamma$  degree of freedom,<sup>9</sup> with  $^{194}\text{Pt}$  particularly soft, so that it has no well-defined shape. This description is consistent with the interacting boson approximation models<sup>10</sup> (IBA-1) which characterize  $^{196}\text{Pt}$  as being at the O(6) symmetry limit of the IBA, a limit which is often referred to as “ $\gamma$  unstable” and which implies zero quadrupole moment for the first excited  $2^+$  level. The nucleus  $^{196}\text{Pt}$  has been shown<sup>11</sup> to have a level scheme and decay spectra consistent with the O(6) limit; but it is  $^{194}\text{Pt}$  which has an excited  $2^+$  level with nearly zero quadrupole moment.<sup>12–15</sup> It is reasonable to expect that the intrinsic structures of these two Pt nuclei are quite similar; the low-energy neutron scattering studies<sup>6–8</sup> argue that the IBA description very near the O(6) limit and similar models are those most appropriate for  $^{194}\text{Pt}$ .

A remarkable finding of the present scattering studies,

as developed further below, is that for  $^{194}\text{Pt}$  the neutron excitation strength is 17% stronger in amplitude, or 37% stronger in scattering probability, than that of Coulomb excitation<sup>12</sup> (CE) or that projected from electromagnetic decay.<sup>16</sup> While, as noted above, small differences between excitation strengths with different probes are not surprising for single-closed-shell nuclei,<sup>2</sup> having only valence protons or valence neutrons, in strongly collective nuclei like the Pt isotopes such a large probe dependence is surprising. We wish to further test the clarity with which the dynamical character of these nuclei can be evoked in neutron scattering.

The purpose of the present 8 MeV neutron scattering study from  $^{190,192}\text{Os}$  and  $^{194}\text{Pt}$  was to test further the striking suggestion that neutron excitation strengths are much stronger than electromagnetic strengths in Pt, and to investigate excitation strengths and structure models in the Os isotopes. If these strength differences are confirmed, then this may suggest that valence proton excitations in  $^{194}\text{Pt}$ , at least, play a different role than valence neutron excitations. Another possibility is that core-polarization effects in nucleon scattering play a role which is not evident under electromagnetic excitation, which does not sense neutrons.

The dynamical character of Pt excitations are interesting for another reason. An earlier study<sup>17</sup> of  $^{12}\text{C}$  scattering from  $^{194}\text{Pt}$  was described in the context of the rigid asymmetric rotor model (ARM), a characterization rather different from that offered by either the O(6) subgroup limit of the IBA, or other  $\gamma$ -soft models. Bound-state studies by Lee *et al.*<sup>18</sup> and model calculations by R. Sahu<sup>19</sup> are also within the context of the ARM, whereas many other studies suggest that  $\gamma$ -soft models are the most appropriate for this shape-transitional region. Brief introductions to the different structure models, tests of them from previous experiments, and our tests with the present neutron scattering cross sections are presented in Sec. III. The experimental systems and methods are presented in Sec. II, the discussion of coupling strengths is in Sec. IV, and Sec. V summarizes our conclusions.

The principal results we have found can be summarized rather simply. First, the earlier suggestion that the  $\gamma$ -soft characterization is most appropriate for  $^{194}\text{Pt}$  is confirmed. There is also striking evidence for an evolution of structure toward triaxiality in proceeding from  $A = 194$  to 190. Neutron-induced transition amplitudes in  $^{194}\text{Pt}$  connecting different scattering channels, though, are rather different from amplitudes found in Coulomb excitation experiments. Our new measurements confirm strong enhancement of neutron-induced quadrupole excitations for that nucleus. What makes these results particularly striking is that the two Os nuclei studied show ground-band quadrupole excitation strengths in neutron scattering equal to those seen in Coulomb excitation. Electric octupole excitation amplitudes for the Os nuclei also are the same for neutron excitation as in CE experiments.

## II. EXPERIMENTAL INSTRUMENTATION AND TECHNIQUES

The present experiment was performed at the tandem accelerator laboratory of the Centre d'Etudes de

Bruyères-le-Châtel. This facility was especially appropriate because of the availability of a high-resolution neutron time-of-flight (TOF) system coupled with a multidetector spectrometer in a low-background scattering hall.<sup>20</sup>

### A. Experimental systems

Accelerated pulsed beams of deuterons were incident on a cylindrical deuterium gas cell to produce neutrons by the  $^2\text{H}(d,n)^3\text{He}$  reaction. The neutrons were then scattered from small, isotopically enriched metallic samples of osmium or platinum into an array of well-shielded detectors placed at laboratory angles ranging between  $20^\circ$  and  $160^\circ$ . Scattered neutron energies were determined via TOF techniques. Various parts of the experimental system have previously been described in detail.<sup>20</sup> The description given here will emphasize those characteristics important for the present measurements.

The incident deuterons were pulsed and bunched with velocity modulation techniques before entering the accelerator. The emerging, high-energy pulsed beam was momentum analyzed and then, approximately 19 m before the deuterium gas cell, entered a post-accelerator bunching system which was phase locked to the arrival of beam pulses. A capacitive beam pickoff placed about 1 m in front of the target sensed the arrival of beam pulses. Beam pulse widths of approximately 0.8 ns were routinely obtained at the target. Typical average currents on target ranged between 3 and  $5.5 \mu\text{A}$ .

The beam entered the deuterium gas cell<sup>20</sup> through a  $2.4 \mu\text{m}$  thick Havar<sup>21</sup> foil. The window was cooled by the deuterium gas itself which was circulated through a refrigerating system and returned to the target cell through a small tube aimed at the window. The deuterium gas cell was 1 cm long and filled to a pressure of approximately 1.5 bar. At the end of the gas cell the beam was stopped on an air-cooled tantalum disk 1 mm thick. The deuteron beam energy at the center of the gas cell was calculated to be 4.75 MeV, based on an energy of 4.95-MeV incident on the gas cell assembly, yielding monoenergetic neutrons of 8.0-MeV energy. Neutrons emerging from the target were incident on a small cylindrical scattering sample of osmium or platinum whose vertical axis was placed  $6.6 \pm 0.1$  cm beyond the end of the cell. The isotopically enriched samples used were obtained from the Isotopes Sales Center at Oak Ridge National Laboratory (ORNL). Details of their isotopic purity, diameter, height, and mass are given in Table I. The

TABLE I. Dimensions and isotopic enrichments of the solid, cylindrical metal scattering samples as used in this work.

Nucleus	Mass (g)	Dimensions (cm)	Enrichment (%)
$^{190}\text{Os}$	38.824	$h = 1.43$ $d = 1.27$	97.8
$^{192}\text{Os}$	66.627	$h = 1.79$ $d = 1.50$	99.1
$^{194}\text{Pt}$	40.120	$h = 1.54$ $d = 1.28$	97.2

sample was supported by thin stainless-steel wires which were hung from a lightweight stainless-steel frame. Each scattering cylinder's alignment with the beam axis and deuterium gas cell was checked with a telescope when samples were interchanged.

The set of neutron detectors used in this work has been previously described.<sup>20</sup> A heavily shielded array of six identical NE213 liquid scintillators 12.7 cm in diameter and 5.1-cm long was placed in the neutron detection hall. The detector array was located on one side of the beam line 8 m from the scattering sample. The six detectors were separated from each other by  $20^\circ$  angular intervals. Each scintillator was coupled to a 10.5 cm diameter XP2041 photomultiplier by a conical light pipe and was placed in a massive tank containing  $\text{Li}_2\text{CO}_3$  to shield against neutrons originating elsewhere in the room. An array of tungsten shadow bars placed close to the scattering sample shielded the scintillators from the neutron production target. The system is illustrated in Fig. 1. The entire assembly of detectors, their shields, and sha-

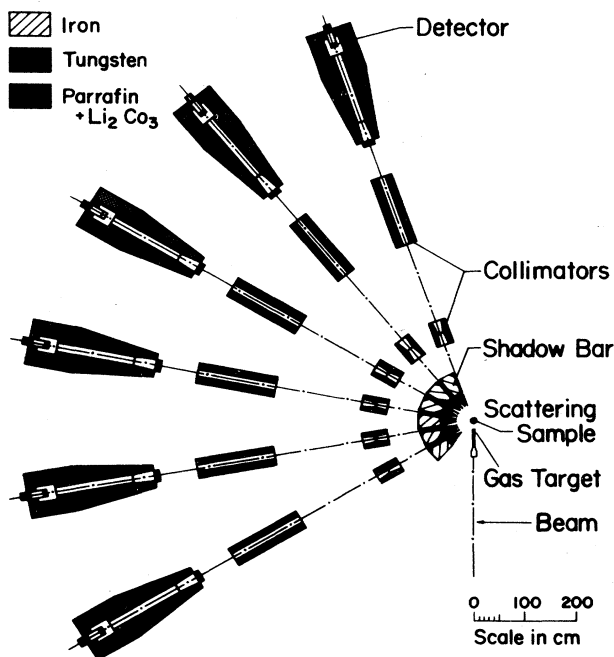


FIG. 1. Target, sample, and detection system. The six-detector system is shown set up for an 8 m flight path. A 3.0-m deep pit extends out to 5 m. The reduced mass steel floor under the gas target, sample, and shadow bar system was to minimize floor rescattered neutrons. The tungsten-tipped steel shadow bars were in a fixed, rotatable assembly. Each detector shield and its intermediate collimators were repositioned and aligned by hand each time the shadow bar assembly was reset to another set of six angles. The six scintillator detectors with photomultipliers were removed from their shields and placed in a separate rack for the short  $0^\circ$  normalization runs.

dow bars was moved periodically to cover the entire angular range between  $20^\circ$  and  $160^\circ$ .

Another detector identical in size and shape was stationary on the opposite side of the beam line at  $-55^\circ$  and at 5 m from the target. It was shielded from room-scattered neutrons but was open to the deuterium gas cell target. Thus, it served as a monitor of the rate of primary neutron production. Normalization of the yields of scattered neutrons in the six movable detectors to this monitor detector's yield eliminated concern about incident beam current integration and constancy of deuterium cell pressure.

Electronics for the detector pulses employed standard pulse-shape discrimination techniques<sup>22</sup> for eliminating  $\gamma$ -ray pulses. Pulse-height and TOF information for neutron events in each detector were stored event by event on magnetic tape. Two on-line spectra were also generated for each detector for observation during the experiment, and were also stored on magnetic disk. Energy thresholds for these spectra were set at 2.5 and 3.5 MeV, respectively. These threshold levels and each neutron detector's gain stability, on which our overall detection efficiency depended, were checked with a radioactive source at 3–4 d intervals and adjusted when necessary over the six weeks the experiment was performed. The overall timing resolution achieved for each detector by itself was 1.0 ns, giving an overall spectral resolution of 1.3 ns, including effects of the angular spread of neutrons incident on the scattering samples, beam pulse width, etc.

A short normalization run was taken with the scattering sample removed for each angular setting of the assembly of six shielded detectors. The six detectors themselves were moved to  $0^\circ$  and 8 m so they all viewed the neutron source directly and simultaneously. This procedure removed the requirement that overall detector efficiencies and incident neutron flux be known. To learn the variation of neutron detection efficiency with energy, the source neutron angular distribution was measured with each detector. The measured yields from the source were then divided by the known cross sections<sup>23</sup> of the  $^2\text{H}(d,n)^3\text{He}$  reaction.

Data were taken by setting the detector angles and shadow bars and then by taking long runs, typically 6–24 h, successively with each of the three scattering samples. During this sequence, another run was taken with the scattering sample removed. At the end of the sequence the short normalization run was taken with the detectors moved to  $0^\circ$ . Six different sets of angles were necessary to cover the entire angular range of the experiment. The settings were arranged so that for each new set of angles one previously taken angle was repeated, to assure consistency between the different angle sets.

## B. Data reduction and uncertainties

The TOF spectra were constructed off line from event-mode tapes, and the spectra were later analyzed interactively. The spectra used for peak-yields analyses were created by subtracting the spectrum for the sample-out run from a run with one of the separated isotope samples. Then, using these difference spectra, the system response

to a single neutron group could be well modeled with  $^{194}\text{Pt}$ , for which the ground-state peak was well separated from the other groups. Each peak in a spectrum was represented by the empirically derived combination of a double Gaussian with an exponential tail and a linear background. The parameters of the peak shape, such as the relative amplitude of the exponential tail, the 8% relative height of the satellite Gaussian relative to that of the main Gaussian, and the distance between the satellite and main Gaussians were fixed to match those extracted from the ground-state fit for  $^{194}\text{Pt}$ . The method of using two Gaussians slightly displaced from each other and of sharply different heights mimics the convolution of Gaussian time spreads with the experimental resolution function, which is asymmetric in time. The parameters of the standard detector response were determined<sup>24</sup> using the fitting program SAN12. The peak-shape parameters for all samples, except for the width of each TOF peak, were fixed to those determined for the  $^{194}\text{Pt}$  ground state. Positions and widths of other peaks in the spectra were fixed by knowing the TOF energy calibration, the kinematical shift in scattered neutron energy versus angle, and the time and energy dispersions  $\Delta t$  and  $\Delta E$  of the source neutrons. Computer searches were made on each spectrum to adjust the heights of the Gaussian peaks to minimize the overall spectrum  $\chi^2$  automatically.

Each detector's yields were normalized to incident neutron fluence with the aid of the  $0^\circ$ , no sample runs. Normalization of inelastic scattering yields requires corrections for variation of the detection efficiency with neutron energy; this is a small correction to the normalization, since except for the  $3^-$  level, scattered neutrons differed from the primary energy of 8 MeV by less than 1 MeV. Even neutrons scattered from the  $3^-$  level were only 1.4 MeV below the elastically scattered neutrons.

The scattering yields, normalized for incident fluence and for neutron detection efficiency, were corrected for sample-size effects. These effects include incoming and outgoing neutron attenuation in the sample, finite geometry, and multiple scattering in the sample. All of these corrections are calculated in the course of simulations using forced collision Monte Carlo methods with the code<sup>25</sup> MULCAT. These corrections have been tested by comparison with analytical methods using the approximations introduced by Engelbrecht<sup>26</sup> and with other Monte Carlo codes.<sup>20</sup>

The most important uncertainty associated with these measurements is that of the stability of neutron detection efficiency over long running periods. Repeated tests led to uncertainties of about  $\pm 3\%$  from that source. Another significant uncertainty is that of the stability of the  $-55^\circ$  monitor. Repeated runs suggest an uncertainty of about  $\pm 2\%$  from that source. The only other large uncertainty is that associated with the statistics of net yields, including peak-fitting uncertainties. These net yield uncertainties are the most important of the relative uncertainties, or those which vary randomly from point to point. The sample-size corrections have very small uncertainties, negligible compared to the ones discussed above except at the minima of the elastic scattering angular distributions, where they contribute  $\pm 3\%$  uncertain-

ties. The normalization uncertainties mentioned above are combined arithmetically to lead to an overall normalization uncertainty  $\pm 5\%$ . This normalization uncertainty is combined in quadrature with the relative uncertainties.

### III. RESULTS AND INTERPRETATIONS: STRUCTURE MODELS

The changing character of the  $\gamma$ -band excitations of these nuclei, and their quite strong collective character, are immediately evident in the neutron velocity spectra, or TOF spectra, shown in Fig. 2. These are scattered neutron spectra for the three nuclei at a laboratory scattering angle of  $105^\circ$ , where elastic scattering is at a relative minimum. It is clear that the  $2_1^+$  excitations are very strong in all three nuclei, the hallmark of nuclei with strong quadrupole collectivity at low-excitation energies.

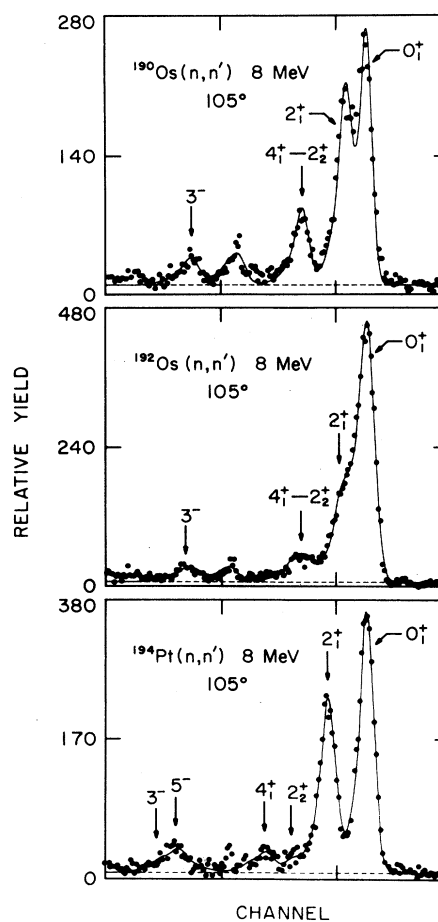


FIG. 2. Typical neutron TOF spectra from  $^{190,192}\text{Os}$  and  $^{194}\text{Pt}$  are shown in the corresponding panels. The scattering groups of interest for each isotope are labeled; background peaks are not labeled. The solid curves were produced by the fitting code SAN12 discussed in the text.

One can see directly, in contrast, that the  $2_2^+$  and  $4_1^+$  excitations are very weak in  $^{194}\text{Pt}$ . Their positions in the spectra are indicated by arrows in Fig. 2. The same two excitations are not resolved in the spectra for the two Os isotopes, but one can easily see there the dramatic difference of these  $\gamma$ -band excitations. The  $2_2^+$  is strongly excited in  $^{192}\text{Os}$  and even more strongly excited in  $^{190}\text{Os}$ , as demonstrated below. There is a very sharp change in  $\gamma$ -band strengths between Os and Pt.

The  $3_1^-$  scattered groups for  $^{190,192}\text{Os}$  were also analyzed. The  $3_1^-$  excitation in  $^{194}\text{Pt}$  could not be separated from a close-lying group; the statistical quality of the data did not permit extracting separate information for the two levels. The contaminant peak unresolved from the  $3_1^-$  peak in the  $^{194}\text{Pt}$  spectra probably is a result of scattering from the  $5^-$  level at 1374 keV in  $^{194}\text{Pt}$ ; other nearby levels may also contribute. The uncertain contribution of levels other than the  $3_1^-$  level made confident extraction of  $\beta_3$  impossible. On the other hand, the width of the  $3_1^-$  peaks in the Os spectra was that expected of a single peak based on the width of the ground-state peak. Further, the peak centroids corresponded to the known  $3_1^-$  excitation energies. No  $^{194}\text{Pt}$  group in the appropriate excitation energy region met these tests. We can, however, compare the  $^{194}\text{Pt}$  neutron TOF spectra with those from  $^{190,192}\text{Os}$  and conclude that the octupole strength observed in  $^{194}\text{Pt}$  is not significantly different from that observed in the Os isotopes. The unlabeled peak lying between the  $4_1^+$  and the  $3_1^-$  excitations in each spectrum arises from incompletely subtracted background, predominantly from  $\gamma$  rays incompletely discriminated against by the pulse-shape discrimination system.<sup>20</sup>

The differential scattering cross sections for the three nuclei are presented in Figs. 3–8. Error bars shown indicate the size of the relative uncertainties. For each sample only three or four resolved peaks could be analyzed, those for the ground state, the  $2_1^+$ -state, the combined  $2_2^+$ -state and  $4_1^+$ -state, and the  $3^-$  state for the Os isotopes. Although the  $2_2^+$ - and  $4_1^+$  states have been resolved for  $^{194}\text{Pt}$ , the statistical error would have been so large for the  $2_2^+$ -state alone that yields for the two states were summed together; this summing was unavoidable for the Os isotopes.

The bombarding energy of the present experiment was chosen to be large enough that the interaction of incident neutrons with heavy nuclei proceeds only via direct coupling mechanisms, or direct interactions. The statistical model or compound nucleus cross sections are negligible.

#### A. General comments—model calculations

Several different nuclear structure models for collective, heavy nuclei describe bound-level energies and especially  $E2$  electromagnetic transition rates. Model parameters were fixed separately for each nucleus. These parametrized models are tested here for the excitation dynamics of these nuclei via neutron scattering. The different models are represented in our analyses by  $E2$  and  $E4$  matrix elements which arise in the calculations of bound-level energies and  $\gamma$ -ray transitions between the levels. The same matrix elements which connect different

bound levels also connect different lepton or hadron channels for scattering from the nuclei. Coupled-channels (CC) calculations, using the reduced matrix elements (RME) as determined by these structure models as input, were carried out and compared with our neutron scattering data. Tests such as these have previously<sup>6–8</sup> shown considerable sensitivity to different collective excitations, especially those of the  $\gamma$  band.

All the models tested except two simple, geometric ones were developed by others to describe nuclear structure in the mass region near  $A = 190$ .<sup>7</sup> Two geometric models were separately parametrized to provide a description of bound-level energies and  $E2$  transition rates in this mass range. All of the models were then applied to our scattering results without any parameter adjustments except for one overall coupling amplitude  $\beta_2$ , which sets the entire quadrupole coupling strength scale. Even  $\beta_2$  is constrained rather tightly by the requirement of providing a good description of total cross sections over the energy range from 0.3 to 30 MeV and the elastic scattering cross sections. A brief introduction to each structure model tested is given below, together with a review of recent tests of these models in earlier experiments and calculations. Models tested were Leander's  $\gamma$  soft,<sup>27</sup> Kumar's DDT,<sup>28,29</sup> IBA-2,<sup>30,31</sup> ARM,<sup>32,33</sup> and RVM.<sup>34</sup> Reduced matrix elements from another model,<sup>35</sup> IBA-1, were also available but only for  $^{194}\text{Pt}$ .

The rigidly deformed asymmetric rotor model is parametrized in terms of two geometric amplitudes,  $\beta$  which characterizes the quadrupole deformation of the nucleus and  $\gamma$  which fixes the departure from axial symmetry of the deformed structure. These two parameters can be fixed to match the ratio of the first and second  $2^+$  excited level energies, or to reproduce the quadrupole moment of the  $2_1^+$  level and the quadrupole excitation strength of that level.<sup>32,33</sup> Since our goal is to test the information content of quadrupole excitation dynamics, we adjusted the parameters to reproduce the  $E2$  strengths. As Sahu noted<sup>19</sup> in his ARM description of Os nuclei, bringing  $E2$  transition rates and level energies into accord with the ARM was successful, except for  $^{192}\text{Os}$ . Our results were similar to his, except that we let the transition rates rather than the level energies fix the parameters. As noted earlier, the parameter  $\beta$  was readjusted slightly during the scattering analyses to optimize the description of the neutron scattering data.

The rotation-vibration model (RVM) is another deformed model, but one which allows vibrational excitations about a deformed, axially symmetric shape.<sup>34</sup> The  $E2$  RME's were calculated<sup>7</sup> to describe level energies and electromagnetic transition rates for each of the nuclei studied here. Thus the critical  $E2$  and  $E4$  matrix elements were unaltered during scattering tests with the model. The ARM and RVM are the two geometric models parametrized by us.  $E2$  and  $E4$  matrix elements were fixed for all models during our tests; they were not variables.

Kumar's dynamic deformation theory (DDT) is a more complete model in that it deals with the complete Bohr Hamiltonian for quadrupole motion. The DDT model had been thoroughly parametrized<sup>28,29</sup> to provide level

energies and electromagnetic transition strengths between levels of many nuclei, including those of this experiment. The reduced matrix elements provided by that parametrization<sup>28,29</sup> were used without modification except that the overall quadrupole coupling amplitude  $\beta_2$  was adjusted to optimize scattering descriptions.

The interacting boson approximation with separate boson excitation schemes for neutrons and protons (IBA-2) had originally been developed to describe nuclei of this mass region<sup>30</sup> and then later redeveloped<sup>31</sup> to provide the best description of these nuclei within the context of that group-symmetry-based model. The subgroup symmetry O(6) form of the IBA-2 was used since that  $\gamma$ -unstable symmetry had been judged particularly appropriate to this shape-transitional mass region in several studies.<sup>30,31</sup> Another form of the interacting boson model which used a single boson basis for both protons and neutrons (IBA-1) had also been parametrized for <sup>194</sup>Pt. The RME's from that model<sup>35</sup> were also tested.

The last model to be described here is the  $\gamma$ -model of Leander.<sup>27</sup> This model was developed to characterize nuclei with potential-energy surfaces which were very "soft" to changes of the  $\gamma$  parameter. Leander separated the Bohr Hamiltonian into terms which depended only on the normal spherical potential and those which corresponded to quadrupole deformation amplitudes. The spherical plus  $\beta$ -dependent parts of the Hamiltonian were solved to provide a deformed basis space in which the  $\gamma$ -dependent perturbation was subsequently calculated. The strength of the  $\gamma$ -dependent perturbation could be varied to provide the best description of the nuclear levels and  $E2$  transition rates. The results are the RME's which characterize the descriptions of this highly successful model.<sup>27</sup>

Another set of matrix elements that were derived not from any model but from an extensive series of Coulomb excitation experiments<sup>2</sup> were available for all three nuclei. These RME's were also used to test the degree of departure of neutron excitations from the electromagnetic ones. The actual  $E2$  and  $E4$  RME's developed from the structure models noted here and the CE RME's are tabulated in other papers<sup>6,36,37</sup> which deal explicitly with the description of total cross sections and differential scattering cross sections at lower energies.

Several earlier studies dealt with the question of the  $\gamma$  rigidity, or deformational rigidity, of the Os and Pt nuclei. The early <sup>12</sup>C scattering studies<sup>17</sup> of <sup>194</sup>Pt were interpreted within the ARM model, but a later study pointed out<sup>38</sup> that the parameters necessary for success with the ARM were inconsistent with the bound-level structure of that nucleus. The development of the O(6) subgroup limit of the IBA models<sup>11</sup> and the microscopic structure model achieved within a constrained Hartree-Fock-Bogoliubov approach<sup>39,40</sup> argue strongly for a  $\gamma$ -soft interpretation of the surface characteristics of these nuclei.

## B. The scattering potentials

The neutron scattering potentials used in these analyses were taken from Ref. 6 for <sup>194</sup>Pt, and from Refs. 7 and 37 for the Os isotopes. Those scattering potentials over

an extended energy region have been carefully determined for <sup>190,192</sup>Os and <sup>194</sup>Pt by requiring fits to total cross sections over the entire region and differential scattering cross sections measured at several incident neutron energies. It is especially important that the scattering potentials be well fixed.

These three neutron scattering potentials are independently found to have almost the same nonlinear energy dependence. Below 5 MeV the potential strengths are essentially energy independent. Above 5 MeV the energy dependence of the potentials is the traditional linear dependence usually found at higher nucleon energies. This nonlinear character reflects dispersion effects in the real part of the scattering potential caused by energy dependencies of the absorptive potentials.<sup>41</sup> The present 8 MeV scattering data are very important in anchoring the energy dependence at this energy. These dispersion effects also illustrate well the connections between bound-state and scattering potentials. The scattering potentials for neutron energies above 5 MeV are presented in Table II.

## C. Model tests for <sup>194</sup>Pt

Considering first <sup>194</sup>Pt, we present the elastic and inelastic scattering to the  $2_1^+$  and  $2_2^+-4_1^+$  levels in Fig. 3. The solid curves in the top two panels of Fig. 3 are representative of CC calculations using any of the nuclear structure models previously mentioned for <sup>194</sup>Pt, except for the RVM.<sup>34</sup> The RVM calculations for elastic scattering were acceptable, but cross sections for the  $2_1^+$  level are much smaller than the solid curve shown in the middle panel of Fig. 3. To constrain a fit to the  $2_1^+$  cross sections using the RVM required changing either the coupling or the scattering potential enough to destroy the fit to the elastic scattering and total cross sections.<sup>6</sup> The concept of entering  $\gamma$ -band excitations through vibrations around a rigid axial shape is quite inconsistent with our measurements for <sup>194</sup>Pt. The reasons for the failure of the RVM are not hard to grasp. A well-deformed structure of this sort leads to strong  $E2$  RME's connecting the  $2_1^+$  to the  $4_1^+$  level via a rotational transition, and to the  $2_2^+$  level via a vibrational transition. The models appropriate for <sup>194</sup>Pt provide very small, almost vanishing,  $E2$  RME's for direct excitation of the  $2_2^+$  level, as is evident in Fig. 2, and small values for coupling between the two  $2^+$  levels.

The scattering data for the  $2_2^+$  and  $4_1^+$  levels are combined, as are the calculations for these two weakly excited levels; both data and calculations are presented in the lower panel of Fig. 3. The curves shown in this figure would be typical of any of the models discussed for <sup>194</sup>Pt. The solid curve which represents the combined calculated cross sections shows little structure, while the measured data can be seen to have a distinct oscillation with angle. The separate components of the combined calculation are plotted as the dashed curve for the  $2_2^+$  and the dot-dashed curve for the  $4_1^+$  levels. The models are not distinguished by these data, in contrast to the results found at lower neutron energies,<sup>6</sup> which showed that only Leander's  $\gamma$ -soft and the IBA-1 models would satisfacto-

TABLE II. The parameter  $E$  or  $E_n$  is the incident neutron energy,  $R$ ,  $R'$ , and  $R^*$  denote radius parameters in the form  $r = RA^{1/3}$ , where  $r$  is the nuclear radius and  $A$  is the mass number. The parameters  $a$  with superscripts denote diffuseness of the different potentials. A constant-volume absorptive potential of the form  $W_v = 0.2 \text{ MeV}$ ,  $R'/a' = 1.26/0.71$  was introduced for all  $E_n > 8 \text{ MeV}$ . The uncertainties quoted for the  $\beta_4$  values come from Refs. 6, 7, and 37.

$^{194}\text{Pt}$ scattering potential parameters for $4.6 \leq E_n \leq 20 \text{ MeV}$			
$V$	$47.2 - 0.39E$	$R/a$	$1.26/(0.59 + 0.12E)$
$W_D$	$2.25 + 0.69E$	$R'/a'$	$1.28/0.47$
$V_{so}$	6.3	$R^*/a^*$	$1.12/0.47$
Deformation parameters: $\beta_2 = -0.17 \pm 0.005$ ; $\beta_4 = -0.04 \pm 0.01$			
$^{192}\text{Os}$ scattering potential parameters for $4.6 \leq E_n \leq 20 \text{ MeV}$			
$V$	$47.0 - 0.36E$	$R/a$	$1.26/(0.59 + 0.12E)$
$W_D$	$2.48 + 0.58E$	$R'/a'$	$1.28/0.47$
$V_{so}$	6.3	$R^*/a^*$	$1.12/0.47$
Deformation parameters: $\beta_2 = 0.15 \pm 0.005$ ; $\beta_4 = -0.03 \pm 0.01$			
$^{190}\text{Os}$ scattering potential parameters for $4.6 \leq E_n \leq 20 \text{ MeV}$			
$V$	$47.0 - 0.36E$	$R/a$	$1.26/(0.59 + 0.12E)$
$W_D$	$2.44 + 0.68E$	$R'/a'$	$1.28/0.47$
$V_{so}$	6.5	$R^*/a^*$	$1.12/0.47$
Deformation parameters: $\beta_2 = 0.168 \pm 0.005$ ; $\beta_4 = -0.03 \pm 0.01$			

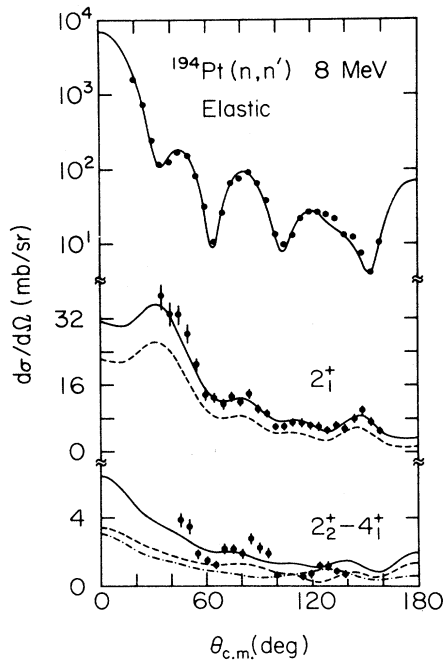


FIG. 3. The scattering cross sections measured at 8 MeV incident energy from  $^{194}\text{Pt}$  are presented. The solid curves represent CC calculations using the CE reduced matrix elements and  $\beta_2 = -0.17$ . The dashed curve plotted with the  $2_1^+$  scattering cross sections was calculated using  $\beta_2 = -0.14$ , the value determined from electromagnetic decay studies.<sup>16</sup> Scattering to the  $2_2^+$  and  $4_1^+$  levels could not be resolved. The dashed and dot-dashed curves for the  $2_2^+ - 4_1^+$  cross sections represent scattering to the  $2_2^+$  and  $4_1^+$  levels, respectively, the solid curve is the sum of the two. Note that linear scales are used in the lower two panels, while a semilog scale is used in the top panel.

rely represent the total and differential scattering cross sections.

#### D. Model tests for $^{192}\text{Os}$

The neutron scattering cross sections from  $^{192}\text{Os}$  are presented in Fig. 4. As for  $^{194}\text{Pt}$ , the elastic and inelastic scattering cross sections to the  $2_1^+$  level were found to be rather insensitive to the particular structure model used in the CC calculations. The solid curves are representative of CC calculations using any of the structure models tested except the RVM (not shown), which gives results too low for scattering to the  $2_1^+$  level. The RVM thus fails badly for  $^{192}\text{Os}$  as it did for  $^{194}\text{Pt}$ ; but its failure is not as severe in this case as it was for  $^{194}\text{Pt}$ . This is because  $\gamma$ -soft models provide much larger  $E2$  RME's for the  $2_2^+$  and  $4_1^+$  levels in  $^{192}\text{Os}$ ; the contrast with the RVM is not as dramatic as it was for  $^{194}\text{Pt}$ . The dashed curve shown with the  $2_1^+$  data is calculated with  $\beta_2 = 0.17$ . Except for the sign, this is the coupling strength needed for  $^{194}\text{Pt}$ . The sensitivity to differences in  $\beta_2$  is apparent.

The inelastic scattering cross sections, especially for the  $2_2^+$  level, were found to be very sensitive to the set of  $E2$  reduced matrix elements used in the CC calculations. The resolution of the experiment was not good enough to separate scattering from the  $2_2^+$  and  $4_1^+$  levels. The experimental cross sections for both levels, as well as the CC calculations presented for them, are combined in the lowest panel of Fig. 4. The component cross sections for the  $2_2^+$  and  $4_1^+$  levels are plotted as dashed and dot-dashed curves, respectively, while the solid curve is the combination of the two. We note that although the cross sections are for both levels, they are now dominated by those for the  $2_2^+$  level. The calculated results for the best model, Leander's  $\gamma$ -soft model,<sup>27</sup> are very similar to the

solid curve shown in the lowest panel of Fig. 4. We see, however, that the best calculation is still well below the measured results. The models, which give reduced matrix elements for direct  $E2$  excitation of the  $2_2^+$  level at least three times as large as the corresponding  $E2$  reduced matrix elements for  $^{194}\text{Pt}$ , still do not provide enough strength to match the sudden jump in  $\gamma$ -band strength in going from  $^{194}\text{Pt}$  to  $^{192}\text{Os}$ . Only Leander's model comes close to being an adequate description of the scattering.

Additional model tests are presented for the  $2_2^+$  and  $4_1^+$  levels of  $^{192}\text{Os}$  in Fig. 5. The solid curve, obtained from the DDT model,<sup>28,29</sup> falls well below the data points. The solid curve of Fig. 5 is also representative of CC calculations using the RVM. The ARM (not shown) fails dramatically to provide enough strength to represent these cross sections. The ARM predicts values which extrapolate to about 4 mb/sr at  $0^\circ$ , or only one half of the ones shown by the solid curve of Fig. 5. Such results also represent the IBA-2 model. None of these models provides an adequate description of neutron scattering from  $^{192}\text{Os}$ , either at this or at lower neutron energies.<sup>37</sup> The results of these 8 MeV tests clearly indicate that  $\gamma$ -rigid

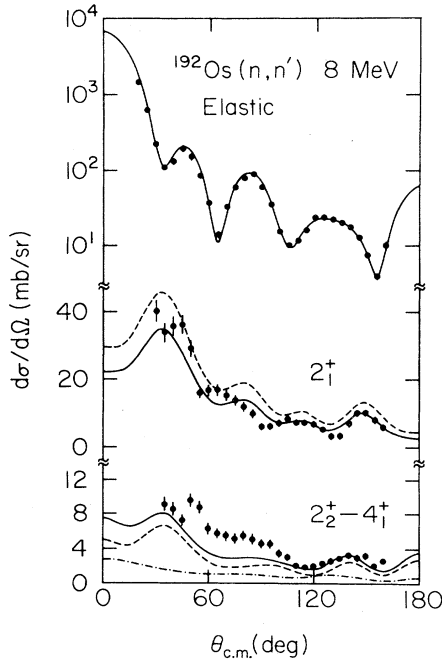


FIG. 4. The scattering cross sections measured at 8 MeV incident energy from  $^{192}\text{Os}$  are presented. The solid curves represent CC calculations using the CE reduced matrix elements and  $\beta_2=0.15$ . The dashed curve plotted with the  $2_1^+$  scattering cross sections was calculated using  $\beta_2=0.17$ ; i.e., the value needed for  $^{194}\text{Pt}$  except for the sign, which is positive for this prolate nucleus. Scattering to the  $2_2^+$  and  $4_1^+$  levels could not be resolved. The dashed and dot-dashed curves for the  $2_2^+$ - $4_1^+$  cross sections represent scattering to the  $2_2^+$  and  $4_1^+$  levels, respectively; the solid curve is the sum of the two. Note that linear scales are used in the lower two panels, while a semilog scale is used in the top panel.

models fail to describe the  $^{192}\text{Os}$  scattering data, and even the much better  $\gamma$ -soft model is inadequate for the  $2_2^+$  level. The dashed curve of Fig. 5 will be discussed in Sec. IV. The best representation of the scattering data comes not from a model, but rather from the reduced matrix elements experimentally derived by Wu *et al.*<sup>12</sup> in CE studies. The calculations for scattering to the  $2_2^+$ - $4_1^+$  levels using the CE RME's are also shown as the solid curve in the lowest panel of Fig. 4.

#### E. Model tests for $^{190}\text{Os}$

The elastic and inelastic scattering cross sections to the  $2_1^+$  and  $2_2^+$ - $4_1^+$  levels of  $^{190}\text{Os}$  measured at 8 MeV incident neutron energy are presented in Fig. 6. All models tested, except the RVM, gave satisfactory results for the elastic and inelastic scattering to the  $2_1^+$  level. The results of the RVM tests are low for the  $2_1^+$  level. Several attempts to improve the fits by increasing  $\beta_2$  were tried, but they degraded the fit to the elastic scattering, indicating that  $\beta_2$  is well fixed. The magnitude of  $\beta_2$  is discussed in more detail in Sec. IV. The RVM calculations, though an inadequate representation, are not as poor a description for  $^{190}\text{Os}$  as for the other two nuclei. As we move from  $^{194}\text{Pt}$  to  $^{190}\text{Os}$  we seem to move gradually toward nuclei for which the RVM would be less deficient.

Calculations for elastic and inelastic scattering to the  $2_1^+$  level from models other than the RVM are shown as solid curves in the top two panels of Fig. 6. The models cannot be distinguished on the basis of these scattering data. Even the ARM, which is dramatically ruled out by examination<sup>37</sup> of total cross sections, provides an adequate description of the  $2_1^+$  cross sections.

Scattering to the  $2_2^+$ - $4_1^+$  levels of  $^{190}\text{Os}$  is presented in the lowest panel of Fig. 6, and again in Fig. 7. The dashed curve of Fig. 6 represents the CC calculation for scattering to the  $2_2^+$  level of  $^{190}\text{Os}$ , while the solid curve would be the sum of cross sections for the two levels. The curves in the lowest panel of Fig. 6 would be

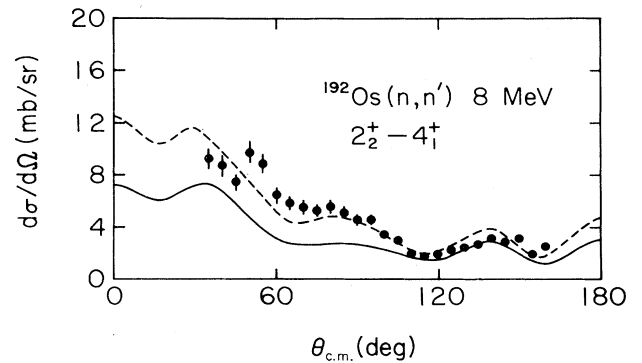


FIG. 5. The scattering cross sections to the  $2_2^+$ - $4_1^+$  levels of  $^{192}\text{Os}$  at 8 MeV incident neutron energy are presented. The solid curve represents a CC calculation using the DDT. The individual  $2_2^+$  and  $4_1^+$  cross sections are not shown. The dashed curve was obtained by increasing the  $E2(0_1^+ \rightarrow 2_2^+)$  matrix element found in EM excitation studies<sup>12</sup> by 33%.

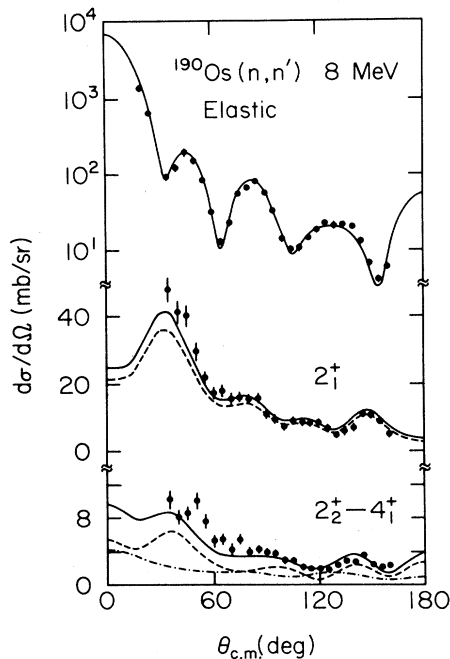


FIG. 6. The scattering cross sections measured at 8 MeV incident energy from  $^{190}\text{Os}$  are presented. The solid curves represent CC calculations using the CE reduced matrix elements and  $\beta_2=0.165$ . The dashed curve for the  $2_1^+$  cross sections results from the RVM model. Scattering to the  $2_2^+$  and  $4_1^+$  levels could not be resolved. The dashed and dot-dashed curves for the  $2_2^+-4_1^+$  cross sections represent scattering to the  $2_2^+$  and  $4_1^+$  levels, respectively; the solid curve is the sum of the two. Note that linear scales are used in the lower two panels, while a semilog scale is used in the top panel.

representative of any of the following models: RVM IBA-2, DDT, or  $\gamma$  soft, as well as the Coulomb excitation reduced matrix elements. Thus, the model discrimination which is so sharp for  $^{192}\text{Os}$  almost vanishes completely for  $^{190}\text{Os}$  at this incident energy. It is particularly notable that the RVM, with its assumption of a stably deformed

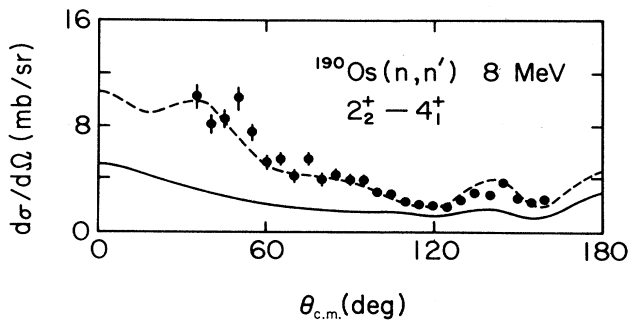


FIG. 7. The scattering cross sections to the  $2_2^+-4_1^+$  levels of  $^{190}\text{Os}$  at 8 MeV incident neutron energy are presented. The solid curve is representative of a CC calculation using the ARM. The individual  $2_2^+$  and  $4_1^+$  cross sections are not shown. The dashed curve was obtained by increasing the  $E2(0_1^+ \rightarrow 2_2^+)$  matrix element found in EM excitation studies<sup>12</sup> by 15%.

axial shape about which  $\gamma$  vibrations occur, becomes close to workable for this nucleus. The exception to the workable models for the  $2_2^+$  cross sections is the ARM, which is plotted as the solid curve in Fig. 7. The ARM fails in  $^{190}\text{Os}$  in the same way that it failed for  $^{192}\text{Os}$ ; i.e., the calculated  $2_2^+$  cross section is much too low.

#### F. Semimicroscopic models for $^{194}\text{Pt}$ and $^{192}\text{Os}$

Semimicroscopic models provide an alternative method of characterizing direct excitations of collective levels. Since we would like to interpret observed coupling strengths quantitatively, and use the model tests of Secs. III B through III D to fix structure properties, further tests of the meaning of coupling parameters  $\beta$  and  $\gamma$  are important.

The electromagnetic excitation strengths for the  $E2$  transitions in the Pt and Os isotopes have been carefully measured in two recent electron scattering studies.<sup>42,43</sup> The resultant  $E2$  strengths are quite consistent with those determined from  $\gamma$ -ray decay studies.<sup>16</sup> The first of the electron scattering studies, a careful and accurate transition strength measurement for  $^{192}\text{Os}$ , also contained a Hartree-Fock calculation of ground-state energies as a function of  $\beta$  and  $\gamma$  using the density-matrix-expansion (DME) method. These calculations showed  $^{194}\text{Pt}$  to be  $\gamma$  unstable, and  $^{192}\text{Os}$  to favor a prolate deformation. Most important for our present purposes, they also provided correct strengths for transitions to the  $2_1^+$  levels. The second electron scattering study,<sup>43</sup> performed on  $^{188,190,192}\text{Os}$  and  $^{194,196}\text{Pt}$  nuclei, included comparisons with calculated cross sections which employed nuclear densities from constrained Hartree-Fock-Bogoliubov (HFB) potential calculations. The self-consistent potential calculations employed the finite-range density-dependent effective force of Gogny.<sup>44,45</sup> These last calculations predicted well the character of the ground states, as the DME calculations had also done.<sup>42</sup> They also gave correct, microscopically based predictions of the  $2_1^+$  strengths. Thus ground states and first excited  $2_1^+$  levels seem well characterized experimentally and theoretically.

Only an extension of the second microscopic calculation, with excited levels based upon a solution to the full Bohr Hamiltonian,<sup>39,45</sup> could predict the  $\gamma$ -band strengths. The HFB calculations were extended in Ref. 43 to calculations of inertial parameters to derive and solve the full Bohr Hamiltonian<sup>28</sup> for quadrupole motion in a consistent, microscopically based manner. The collective amplitudes calculated in this manner have a virtue that the  $\beta$  and  $\gamma$  values no longer have to be specified externally as structure properties. The calculated  $2_2^+$  strengths<sup>43</sup> from the extended HFB model were too weak as compared to the measured electron scattering cross sections.

The constrained HFB calculations<sup>40,45,46</sup> also yielded a potential-energy surface insensitive to changes in nuclear shape. That is, they produced potential surfaces consistent with the conclusions of this and earlier scattering studies that the Os and Pt region was one of ill-defined nuclear shape, best described with the  $\gamma$ -soft models favored in the phenomenological model tests above.

The semimicroscopic, collective excitation amplitudes are folded in with a Woods-Saxon scattering potential whose parameters were essentially those of Table II, producing the transition form factors to be used in CC calculations for neutron scattering from  $^{194}\text{Pt}$  and  $^{192}\text{Os}$  nuclei.<sup>40,46</sup> Cross sections from these calculations are shown in Fig. 8 as the solid curves together with measured cross sections and also the calculations from the phenomenological DDT model of Fig. 4 for  $^{192}\text{Os}$ . The latter are shown as the dashed curves. The phenomenological model had required the insertion of  $E2$  and  $E4$  matrix elements in place of the excitation amplitudes, and has two adjustable structure parameters,  $\beta_2$  and  $\beta_4$ . The HFB-based calculations do not describe the detailed angle dependence of the measured elastic and inelastic scattering cross sections as well as the phenomenological ones do, but the semimicroscopic model tested this way has no free parameters. The extended HFB results of Fig. 8 miss the second minimum and back-angle cross sections for elastic scattering, are too large for the  $2_1^+$  level, and too weak for the  $2_2^+$  level, but the overall description is reasonable, except for the  $2_2^+$  level, for which none of the models provides an adequate description.

These same semimicroscopic calculations are also made<sup>46,47</sup> for  $^{194}\text{Pt}$ , and in that case they are almost indistinguishable from those for the macroscopic DDT model of Fig. 3. The comparisons between the extended HFB model and the phenomenological models for these two nuclei are encouraging; the two methods of testing collective models of these nuclei give essentially the same re-

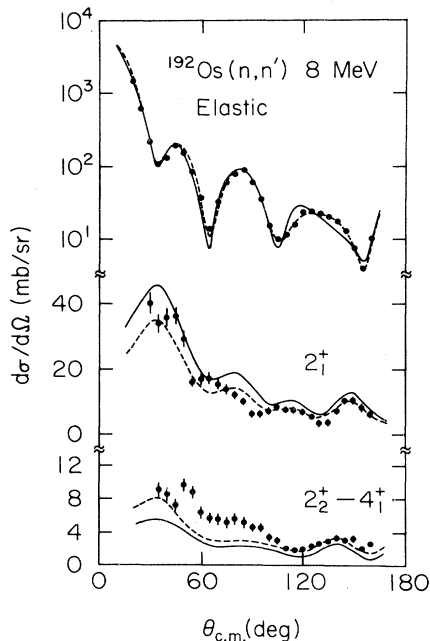


FIG. 8. The scattering cross sections measured at 8 MeV incident neutron energy from  $^{192}\text{Os}$  are shown with HFB-extended theoretical calculations discussed in Sec. III F. The dashed curves repeat the DDT phenomenological model calculations shown in Fig. 4, for comparison of phenomenological and semimicroscopic models.

sults; the comparison shows the consistency of the usual interpretation of coupling strengths using phenomenological models, characterized by fitted values for the parameters  $\beta$  and  $\gamma$ .

There were several reasons for selecting  $^{192}\text{Os}$  and  $^{194}\text{Pt}$  for this comparison. The model calculations shown earlier for the  $2_2^+$  levels of these two nuclei in the DDT framework were unsatisfactory, in different ways for the two nuclei. The present semimicroscopic calculations suggest that those deficiencies do not have to do with the approximations involved in making the analyses, but are intrinsic to the DDT model itself. Another interesting and satisfactory result is that the semimicroscopic calculations have been made using two slightly different numerical methods and two different computer codes.<sup>40,46,47</sup> The results of calculations for the two methods are indistinguishable from each other; this provides an excellent test of these computational methods.

#### IV. COUPLING STRENGTHS AND NUCLEAR DYNAMICS

##### A. Ground-state-band coupling strengths

Coupled-channels calculations for the elastic and inelastic scattering cross sections to the  $2_1^+$  level of  $^{190,192}\text{Os}$  and  $^{194}\text{Pt}$  were found to be almost model independent for the models tested. Further, compound nuclear cross sections are negligible at 8 MeV incident energy for Os and Pt. Thus, this should be an ideal energy for determining the quadrupole coupling strength  $\beta_2$  needed to describe neutron scattering. The method used for determining  $\beta_2$  is as follows. The neutron elastic scattering cross sections for each isotope as well as the total cross sections were fit with the computer code<sup>48</sup> ECIS79 using several values of  $\beta_2$ . For each value of  $\beta_2$ , the surface imaginary potential was varied such that the elastic scattering was well fit; in addition, best results were found when the volume imaginary potential was slightly nonzero, though it played a very small role in the cross-section determinations.

The fits to the elastic scattering cross sections are shown in Figs. 3–6. The corresponding fits to scattering to the  $2_1^+$  levels could then be compared with the measured cross sections and the optimum values of  $\beta_2$  could be determined. Comparisons of such calculations are shown in the middle panels of Figs. 3 and 4 as solid and dashed curves; the solid curves represent the best fits to the measured data. The quadrupole coupling strengths  $\beta_2$  determined from these data are 0.165, 0.15, and  $-0.17$  for  $^{190}\text{Os}$ ,  $^{192}\text{Os}$ , and  $^{194}\text{Pt}$ , respectively. The dashed curve shown in Fig. 3 for the  $2_1^+$  level of  $^{194}\text{Pt}$  shows the cross sections for  $\beta_2 = -0.14$ , about the value deduced from CE. We see that the calculations for that  $\beta_2$  fall far below the data. Even a value of  $\beta_2 = -0.16$  leads to calculated cross sections well below the measured values. For contrast, the dashed curve shown in Fig. 4 for the  $2_1^+$  level of  $^{192}\text{Os}$  illustrates calculations for  $\beta_2 = 0.17$ , a value 13% larger than the proper value for that nucleus. This curve is too large; this is particularly evident for angles beyond  $60^\circ$ .

Conversely, tests could be done fixing the value of  $\beta_2$ , and then the surface imaginary potential,  $W_D$ , could be varied until the inelastic scattering cross sections for the  $2_1^+$  level were well fit. For example, an effort to achieve a fit to the  $2_1^+$  cross sections for  $^{194}\text{Pt}$  was made in this manner by decreasing  $W_D$  which allowed a corresponding decrease in  $\beta_2$ . But decreasing  $W_D$  yielded calculated elastic scattering cross sections much larger than the measurements. Lowering  $W_D$  also led to very poor calculations for the total cross sections. Thus, it was not possible to alter the  $\beta_2$  values found for these nuclei as much as 10% without severely damaging the fits to other well-measured scattering observables, particularly the total and elastic scattering cross sections. This sensitivity study shows that the well-known  $W\beta$  ambiguity traditionally observed in optical-model studies is nearly removed by demanding that the CC calculations reproduce simultaneously many scattering observables. The uncertainties quoted in Table II for the  $\beta_2$  values derive from tests in which different  $\beta_2$  values were set, and other parameters searched to maintain a fit to differential cross sections for both elastic scattering and inelastic scattering to the  $2_1^+$  level and the total cross sections as a function of energy. These tests<sup>7</sup> showed conclusively that  $\beta_2$  values were tightly constrained if either elastic or inelastic scattering cross sections were not to be poorly represented. As noted above, the potential parameter most tightly coupled to  $\beta_2$  values was  $W_D$ . These uncertainties are also consistent with those found in lower-energy scattering studies.<sup>6,37</sup>

The quadrupole coupling strengths  $\beta_2$  can be compared to those found in other studies. The neutron scattering values of  $\beta_2$  for  $^{190,192}\text{Os}$  are in good agreement with Coulomb excitation<sup>12</sup> and  $\gamma$ -ray decay studies.<sup>16</sup> Experience has shown us that the quadrupole coupling strength for deformed collective nuclei is not probe dependent. Thus, we interpret the ground-band excitation dynamics of these Os isotopes as those of deformed nuclei. On the other hand, nuclei not deformed, such as  $^{194}\text{Pt}$ , and spherical nuclei near closed shells often<sup>2</sup> show a large probe dependence for  $\beta_2$ . This is because the target protons and neutrons are not strongly coupled to each other. Thus, in the language of IBA-2 symmetries,<sup>30,31</sup>  $F$ -spin symmetry is not fully conserved, even for the lowest-lying  $2^+$  level.

The quadrupole coupling strength  $\beta_2$  for  $^{194}\text{Pt}$  has previously been shown<sup>6</sup> in neutron scattering to be considerably larger than found in Coulomb excitation and  $\gamma$ -ray decay studies.<sup>16</sup> That result<sup>6</sup> is confirmed here. Unlike the stably deformed Os isotopes, whose first excited states have large quadrupole moments, the first excited state of  $^{194}\text{Pt}$  has a quadrupole moment very close to zero.<sup>13,49</sup> Thus, it should not be surprising to find that target neutrons and protons do not act coherently.

To make these calculations for all models properly complete, single-step  $E4$  amplitudes were included with the quadrupole amplitudes discussed above. Many test calculations showed that the elastic and inelastic scattering cross sections were not very sensitive to the precise values of the  $E4$  matrix elements used for those calcula-

tions, or to the  $\beta_4$  values. The  $\beta_4$  values used were taken from the electron scattering studies of Reuter *et al.*<sup>42</sup> These values had enabled a good description of the differential scattering cross sections for the  $4_1^+$  level and total cross sections measured<sup>6,37</sup> for incident neutron energies near 4 MeV as well as for electron scattering.<sup>42</sup> Since the nuclear structure models tested do not provide  $E4$  RME's, we used those provided by the IBA-1 model of Deason *et al.*<sup>35</sup> as well as values taken from CE experiments.<sup>12</sup> None of the conclusions above regarding  $E2$  coupling strengths or model dependencies are sensitive to reasonable variations of these  $E4$  matrix elements. Since we did not separate the  $2_2^+$  and  $4_1^+$  levels, and since our  $E2$  coupling tests were rather insensitive to the  $E4$  amplitudes, the  $\beta_4$  values were constrained little in this analysis; tests similar to those for determining the  $\beta_2$  uncertainties were also applied for  $\beta_4$  values, with the resulting uncertainty of  $\pm 0.03$ . However, other scattering experiments carried out at lower energy<sup>6,37</sup> did lead to separated differential scattering cross sections for the  $4_1^+$  level. These experiments resulted in uncertainties of  $\pm 0.01$ ; this is the value quoted in Table II, to avoid entering different uncertainties and confusion from different experiments.

Comparisons of coupling strengths between analyses of different experiments should be in terms of deformation lengths  $\beta R$ , since that is the expansion parameter for the surface couplings appropriate to these low-energy nuclear excitations. All comparisons offered here are in terms of the coupling amplitudes  $\beta_i$ . However, the  $\beta_i$  from different experiments have been carefully rescaled to reflect radius differences of the analyses being compared. Thus all  $\beta$  comparisons are referred to the geometry of this and previous<sup>6</sup> neutron scattering analyses, given in Table II.

### B. Gamma-band coupling strengths

The direct, one-step excitation of the  $\gamma$  bandhead in  $^{194}\text{Pt}$  is so weak that the calculated cross sections are dominated by the two-step process through the  $2_1^+$  level. The calculated magnitudes for the combined  $2_2^+$  and  $4_1^+$  level cross sections are shown in Fig. 3; the average magnitude is correct, but the angle-dependent structure is not reproduced. This is probably a result of inadequate treatment of the very weak one-step excitation of the  $\gamma$  bandhead, as noted earlier.

As noted in connection with Fig. 2, the strength associated with excitation of the  $2_2^+$  levels in the Os isotopes is much larger than that for the Pt isotopes; there is a dramatic shift to nonaxial character of the dynamics of these nuclei. This is reflected in the several  $\gamma$ -soft models appropriate for these nuclei, which produce large  $E2(0_1^+ \rightarrow 2_2^+)$  RME's for them, approximately four to five times larger than that for  $^{194}\text{Pt}$ . This difference is immediately evident in the lowest panels of Figs. 3, 4, and 6. The calculations for the two Os isotopes and the measurements are very different from those for  $^{194}\text{Pt}$ .

The solid curves of Figs. 4 and 6 are produced by taking the Coulomb excitation (or electron scattering)  $E2$  re-

duced matrix elements and inserting them into the coupled-channels description of neutron scattering, as noted earlier. For the Os isotopes the ground state and  $2_1^+$  scattering cross sections are well described in this manner. But the solid curves in the lowest panels of those figures are too low, particularly so for  $^{192}\text{Os}$ . The carefully developed Hartree-Fock<sup>42</sup> and HFB models<sup>43</sup> produced  $2_2^+$  cross sections too small to fit electromagnetic excitations. Hence the HFB calculations would be much too small for our neutron scattering measurements. This is directly illustrated in Fig. 8, which shows the measured neutron scattering cross sections once again for  $^{192}\text{Os}$  and CC predictions as obtained using<sup>40</sup> the collective wave functions deduced in Refs. 39 and 43 from the full Bohr Hamiltonian.

The dashed curves of Fig. 5 and 7, which finally do provide a good description of cross sections to the  $2_2^+$  levels of the two Os nuclei, are produced in another way. Here we have arbitrarily increased the  $E2(0_1^+ \rightarrow 2_2^+)$  reduced matrix element above that found in CE studies by 33% for  $^{192}\text{Os}$  and about 15% ( $^{190}\text{Os}$ ). Thus, a possible interpretation of these excitations arises. Instead of thinking of these as surface excitations, one treats them as dominated by valence protons and neutrons. Collective excitations which preserve good neutron-proton symmetry are those of the IBA-1 models, which use a single basis space for both proton and neutron bosons. The language of  $F$ -spin symmetry<sup>31</sup> classifies such excitations as belonging to the lowest  $F$  spin. This symmetry would be rather strongly broken for the  $2_2^+$  excitation of  $^{192}\text{Os}$ , and somewhat less broken for the same excitation of  $^{190}\text{Os}$ . This is reminiscent of the similar finding above of symmetry breaking for excitation of  $2_1^+$  excitations of  $^{194,196}\text{Pt}$ , while symmetry is preserved for  $2_1^+$  excitations of  $^{190,192}\text{Os}$ . The  $\gamma$ -band results now show similar departures from  $F$ -spin symmetry in the  $2_2^+$  excitations in the Os isotopes, where those excitations are evolving in strength very rapidly.

### C. Octupole strengths in Os isotopes

Reuter *et al.*<sup>42</sup> and Boeglin *et al.*<sup>43</sup> examined the electron scattering strength to the lowest  $3_1^-$  level of  $^{192}\text{Os}$  and found a  $B(E3)$  value of  $0.13 e^2 b^3$ . This corresponds to a coupling parameter of  $\beta_3=0.06$ , after scaling to the potential radius which we have used for our neutron scattering analyses. The neutron scattering cross sections to the  $3_1^-$  levels of both  $^{190}\text{Os}$  and  $^{192}\text{Os}$  are shown in Fig. 9, with the  $^{192}\text{Os}$  results shown in the upper panel. The solid curves shown there for both isotopes are obtained assuming  $\beta_3=0.06$ . These result from CC calculations in which the  $3_1^-$  levels are included as harmonic vibrations, with the ground-state band and  $\gamma$ -band excitations calculated using CE matrix elements; that is, the even-parity levels were treated just as for the tests discussed in Sec. III. The calculated  $3_1^-$  cross sections are not sensitive to the sign of  $\beta_3$ , since the  $3^-$  vibration is treated in first order. The dashed curves are calculated for  $\beta_3=0.07$  and  $0.04$  for  $^{192}\text{Os}$  and  $^{190}\text{Os}$ , respectively. These two calculations are presented to illustrate the sensitivity of the cross sections to the size of the coupling parameter. Thus, as

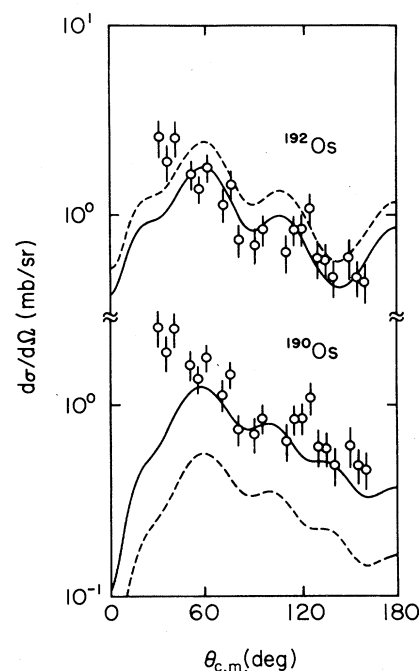


FIG. 9. Inelastic scattering cross sections from the  $3_1^-$  levels of  $^{192}\text{Os}$  and  $^{190}\text{Os}$  are shown in the upper and lower panels, respectively. The solid curves represent CC calculations which use the coupling strength  $\beta_3=0.06$  for both isotopes. The dashed curve in the top panel for  $^{192}\text{Os}$  was calculated using  $\beta_3=0.07$ ; the dashed curve in the lower panel was calculated us-

for the strengths to the  $2_1^+$  excitations of the Os isotopes, the neutron scattering octupole strengths are well determined and are just those from CE or electron scattering cross sections.

The random-phase approximation (RPA) calculations of  $E3$  strengths in  $^{190,192}\text{Os}$  by Neergard and Vogel<sup>50</sup> provide just the strength shown in Fig. 9 with  $\beta_3=0.06$ . These authors conjectured that the  $E3$  strength would vary little in the Os isotopes; our results for the two Os isotopes are quite consistent with those projections. These  $E3$  strengths are much weaker than those found for the Pb isotopes.<sup>51</sup> This is also consistent with the modeling<sup>50</sup> which proposes that the  $E3$  strength of the spherical Pb nuclei is fragmented by coupling to the quadrupole deformation in the Os nuclei. The small variation of the  $E3$  strengths between the two isotopes reflects the fact that the quadrupole moments of the  $2_1^+$  levels are not very different.<sup>13,49</sup>

## V. CONCLUSIONS

The  $^{190,192}\text{Os}$  and  $^{194}\text{Pt}$  scattering cross sections measured at 8 MeV illustrate the rapidly evolving character of the electric quadrupole dynamics of these shape-transitional nuclei. All these nuclei are best characterized as having dynamic triaxiality. The Os isotopes show the same electric quadrupole strengths in neutron scattering as is seen with electromagnetic excitation for the ground-band  $E2$  transitions. This is usually what is

found for deformed nuclei. However, the nonaxial or  $\gamma$ -band  $E2$  excitations, suddenly sharply increased from those in Pt isotopes, do show probe-dependent strengths, suggesting that target neutrons and protons participate differently in these excitations. The  $E3$  excitations, treated as harmonic vibrations, show strengths for neutrons similar to those found with electromagnetic probes in  $^{190}\text{Os}$  and  $^{192}\text{Os}$ ; they behave as do the ground-band  $E2$  excitations. Thus, the valence space effects associated with the probe-variable nonaxial  $E2$  effects are not present for the  $E3$  excitations in the Os isotopes.

The  $^{194}\text{Pt}$  ground-band strengths seen in lower-energy neutron scattering were reported<sup>6</sup> to be considerably stronger than those observed in CE studies. This result is confirmed here. The data did not permit extraction of octupole strengths for  $^{194}\text{Pt}$ ; thus whether the valence space effects associated with the probe-variable  $E2$

strengths would also be present in the  $E3$  excitations could not be ascertained.

#### ACKNOWLEDGMENTS

Two of the authors, (M.T.M. and T.B.C.) would like to thank their hosts at Centre d'Etudes Nucléaires de Bruyères-le-Châtel, and especially J. Lachkar, now of the Centre d'Etudes de Limeil, for their enthusiastic support and kind hospitality during this experiment. The technical assistance of J. P. Lochard, S. Seguin, C. Humeau, and Y. de Penquer during the six continuous weeks of data collection is gratefully acknowledged. This work was partially supported by the U.S. Department of Energy, Office of High Energy and Nuclear Physics, under Contract Nos. DE-AC05-76ER1067 and DE-AS05-76ER2408 and by the National Science Foundation under Grant No. PHY-8702369.

\*Permanent address: Department of Physics and Astronomy, University of North Carolina, Chapel Hill, NC 27599-3255 and Triangle Universities Nuclear Laboratory, Durham, NC 27706.

†Permanent address: IBM E/S National Support Center, 1503 LBJ Freeway, Dallas, TX 75234-6032.

‡Permanent address: Institute of Atomic Physics, Beijing, People's Republic of China.

<sup>1</sup>R. W. Finlay, J. Rapaport, M. H. Hadizadeh, M. Mirzaa, and D. E. Bainum, Nucl. Phys. **A338**, 45 (1980).

<sup>2</sup>A. M. Bernstein, V. R. Brown, and V. A. Madsen, Comments Nucl. Part. Phys. **11**, 203 (1983), and references cited therein.

<sup>3</sup>R. S. Mackintosh, Nucl. Phys. **A266**, 379 (1976).

<sup>4</sup>M. T. McEllistrem, R. E. Shamu, J. Lachkar, G. Haouat, Ch. Lagrange, Y. Patin, J. Sigaud, and F. Cocu, Phys. Rev. **C 15**, 927 (1977).

<sup>5</sup>J. P. Delaroche, G. Haout, J. Lachkar, Y. Patin, J. Sigaud, J. Chardine, Phys. Rev. **C 23**, 136 (1981).

<sup>6</sup>S. E. Hicks, J. P. Delaroche, M. C. Mirzaa, J. Hanly, and M. T. McEllistrem, Phys. Rev. **C 36**, 73 (1987).

<sup>7</sup>Steven E. Hicks, Ph.D. dissertation, University of Kentucky, 1987.

<sup>8</sup>M. C. Mirzaa, J. P. Delaroche, J. L. Weil, J. Hanly, and M. T. McEllistrem, Phys. Rev. **C 32**, 1488 (1985).

<sup>9</sup>L. Wilets and M. Jean, Phys. Rev. **102**, 788 (1956).

<sup>10</sup>R. F. Casten and J. A. Cizewski, Nucl. Phys. **A309**, 477 (1978).

<sup>11</sup>R. F. Casten and D. D. Warner, Rev. Mod. Phys. **60**, 389 (1988), and references cited therein.

<sup>12</sup>Ching-Yen Wu, Ph.D. dissertation, University of Rochester, 1983; D. Cline, Annu. Rev. Nucl. Part. Sci. **36**, 683 (1986); D. Cline (private communication).

<sup>13</sup>C. Y. Chen, J. X. Saladin, and Abdul A. Hussein, Phys. Rev. **C 28**, 1570 (1983).

<sup>14</sup>G. Y. Gyapong, R. H. Spear, M. T. Esat, M. P. Fewell, A. M. Baxter, and S. M. Burnett, Nucl. Phys. **A458**, 165 (1986).

<sup>15</sup>M. V. Hoehn, E. B. Shera, H. D. Wohlfahrt, Y. Yamazaki, and R. M. Steffen, Bull. Am. Phys. Soc. **24**, 53 (1979).

<sup>16</sup>S. Raman, C. H. Malarkey, W. T. Milner, C. W. Nestor, Jr., and P. H. Stelson, At. Data Nucl. Data Tables **36**, 1 (1987).

<sup>17</sup>F. T. Baker, A. Scott, T. P. Cleary, J. L. C. Ford, E. E. Gross, and D. C. Hensley, Nucl. Phys. **A321**, 222 (1979); F. T. Baker,

*ibid.* **A331**, 39 (1979).

<sup>18</sup>I. Y. Lee, D. Cline, P. A. Butler, R. M. Diamond, J. O. Rasmussen, R. S. Simon, and F. S. Stephens, Phys. Rev. Lett. **39**, 684 (1977).

<sup>19</sup>R. Sahu, Phys. Rev. **C 29**, 1486 (1984).

<sup>20</sup>J. Lachkar, M. T. McEllistrem, G. Haouat, Y. Patin, J. Sigaud, and F. Cocu, Phys. Rev. **C 14**, 933 (1976); G. Haouat, J. Lachkar, J. Sigaud, Y. Patin, and F. Cocu, Nucl. Sci. Eng. **65**, 331 (1978); G. Haouat, J. Lachkar, Ch. Lagrange, J. Jary, J. Sigaud, and Y. Patin, *ibid.* **81**, 491 (1982).

<sup>21</sup>Precision Foils Division, Hamilton Technology, Lancaster, PA.

<sup>22</sup>D. W. Glasgow, D. E. Vekley, J. D. Brandenberger, and M. T. McEllistrem, Nucl. Instrum. Methods **114**, 535 (1974).

<sup>23</sup>H. Liskien and A. Paulsen, Nucl. Data Tables **15**, 57 (1975).

<sup>24</sup>Sally F. Hicks, S. E. Hicks, J. Hanly, and M. T. McEllistrem, (submitted to Comput. Phys. Commun.; this program is available at Physics and Astronomy, University of Kentucky, Lexington, KY 40506.)

<sup>25</sup>D. E. Vekley, D. W. Glasgow, J. D. Brandenberger, and M. T. McEllistrem, Nucl. Instrum. Methods **129**, 231 (1975); John R. Lilley, Service de Physique et Techniques Nucleaires, Centre d'Etudes de Bruyères-le-Châtel, Report No. P2N/934/80 (1980).

<sup>26</sup>C. A. Engelbrecht, Nucl. Instrum. Methods **80**, 187 (1970); **93**, 103 (1971).

<sup>27</sup>G. Leander, Nucl. Phys. **A273**, 286 (1976).

<sup>28</sup>K. Kumar and M. Baranger, Nucl. Phys. **A 92**, 608 (1967); K. Kumar, B. Remaud, P. Aguer, J. S. Vaagen, A. C. Rester, R. Foucher, and J. H. Hamilton, Phys. Rev. **C 16**, 1235 (1977).

<sup>29</sup>K. Kumar, Phys. Lett. **29B**, 25 (1969).

<sup>30</sup>R. Bijker, A. E. L. Dieperink, O. Scholten, and R. E. Spanhoff, Nucl. Phys. **A344**, 207 (1980); R. Bijker (private communication).

<sup>31</sup>A. E. L. Dieperink, in *Collective Bands in Nuclei*, edited by D. Wilkinson (Pergamon, New York, 1983), p. 121.

<sup>32</sup>A. S. Davydov and G. F. Filippov, Nucl. Phys. **8**, 237 (1958); A. S. Davydov and A. A. Chaban, *ibid.* **20**, 499 (1960).

<sup>33</sup>A. S. Davydov and V. S. Rostovsky, Nucl. Phys. **12**, 58 (1959).

<sup>34</sup>A. Faessler, W. Greiner, and R. K. Sheline, Nucl. Phys. **70**, 33 (1965); see also J. P. Delaroche, Phys. Rev. **C 26**, 1899 (1982).

- <sup>35</sup>P. T. Deason, C. H. King, R. M. Ronningen, T. L. Khoo, F. M. Bernthal, and J. A. Nolan, *Phys. Rev. C* **23**, 1414 (1981); P. T. Deason, Jr., Ph.D. dissertation, Michigan State University, 1979.
- <sup>36</sup>S. E. Hicks, Z. Cao, J. Sa, J. L. Weil, and M. T. McEllistrem (submitted to *Phys. Rev. C*).
- <sup>37</sup>S. E. Hicks, Z. Cao, M. C. Mirzaa, J. Sa, J. L. Weil, and M. T. McEllistrem (submitted to *Phys. Rev. C*).
- <sup>38</sup>H. L. Yadav, B. Castel, and H. Toki, *Phys. Rev. C* **22**, 2644 (1980).
- <sup>39</sup>M. Girod and B. Grammaticos, *Phys. Rev. Lett.* **40**, 361 (1978); M. Girod, in Proceedings of the Conference of the Specialists Meeting on the Use of the Optical Model for the Calculation of Neutron Cross sections below 20 MeV, [Organization for Economic Cooperation and Development (OECD) Report No. NEANDC-222U, 1986].
- <sup>40</sup>J. P. Delaroche and F. S. Dietrich, *Phys. Rev. C* **35**, 942 (1987).
- <sup>41</sup>S. E. Hicks and M. T. McEllistrem, *Phys. Rev. C* **37**, 1787 (1988).
- <sup>42</sup>W. Reuter, E. B. Shera, M. V. Hoehn, F. W. Hersman, T. Milliman, J. M. Finn, C. Hyde-Wright, R. Lourie, B. Pugh, and W. Bertozzi, *Phys. Rev. C* **30**, 1465 (1984).
- <sup>43</sup>W. Boeglin, P. Egelhof, I. Sick, J. M. Cavedon, B. Frois, D. Goutte, X. H. Phan, S. K. Platchkov, S. Williamson, and M. Girod, *Phys. Lett.* **B186**, 285 (1987); *Nucl. Phys.* **A477**, 399 (1988).
- <sup>44</sup>D. Gogny, in *Nuclear Self-Consistent Fields*, edited by G. Ripka and M. Porneuf (North-Holland, Amsterdam, 1982).
- <sup>45</sup>J. Decharge and D. Gogny, *Phys. Rev. C* **21**, 1568 (1980); M. Girod and B. Grammaticos, *ibid.* **C 27**, 2317 (1983).
- <sup>46</sup>K. Kumar, Ch. Lagrange, M. Girod, and B. Grammaticos, *Phys. Rev. C* **31**, 762 (1985).
- <sup>47</sup>Ch. Lagrange, D. G. Madland, and M. Girod, *Phys. Rev. C* **33**, 1616 (1986).
- <sup>48</sup>J. Raynal, ECIS79 (unpublished); *Computing as a Language of Physics* (IAEA, Vienna, 1972); *The Structure of Nuclei* (IAEA, Vienna, 1972), p. 75; *Phys. Rev. C* **23**, 2571 (1981).
- <sup>49</sup>M. V. Hoehn, E. B. Shera, H. D. Wohlfahrt, Y. Yamazaki, and R. M. Steffen, *Phys. Rev. C* **24**, 1667 (1981).
- <sup>50</sup>K. Neergard and P. Vogel, *Nucl. Phys.* **A145**, 33 (1970).
- <sup>51</sup>S. E. Hicks, G. R. Shen, J. M. Hanly, Sally F. Hicks, and M. T. McEllistrem (unpublished).